Hybrid Control Scheme for Photovoltaic Micro-Inverter with Adaptive Inductor

Jiarong Kan[1], *Member, IEEE*, Yunya Wu[1], Yu Tang[2], Senior *Member, IEEE*, Shaojun Xie[3], *Member, IEEE*, and Lin Jiang[4], *Member, IEEE*
(e-mail: kanjr@163.com, wuyunyayancheng@126.com, ty8025@hotmail.com,eeac@nuaa.edu.cn, ljiang@liv.ac.u)
1. College of electrical engineering, Yancheng Institute of Technology Yancheng, 224053, China
2. State Key Laboratory of Reliability and Intelligence of Electrical Equipment（Hebei University of Technology）& Key Laboratory of Electromagnetic Field and Electrical Apparatus Reliability of Hebei Province(Hebei University of Technology), Tianjin, 300401, China
3. College of Automation Engineering, Nanjing University of Aeronautics and Astronautics Nanjing, 210016, China
4. Department of Electrical Engineering and Electronics, The University of Liverpool, Liverpool, L69 3GJ, U.K.

Abstract- This paper studies a two-stage PV micro-inverter. Its prestage is a full-bridge DC-DC converter with an adaptive inductor whose inductance can be regulated by a controlled current source. The aim of the adaptive inductor is to realize current boundary continuous mode (BCM) operation with constant-frequency (CF) and decrease the current stress of the switches in the prestage converter. The structure and operational principle of the proposed adaptive inductor are introduced. The mathematical model has been established for achieving the proper inductance of the adaptive inductor for BCM operation and for verifying the operational condition of the core. The current stress of switches and power loss of the prestage converter with the adaptive inductor or the fixed inductor are analyzed. A hybrid control strategy, which includes the adaptive inductor regulating, discontinuous conduction mode (DCM) or BCM selection in different power range, is proposed according to the derived mathematical model. The experimental results are presented to verify the analysis.

Index Terms- PV micro-inverter; adaptive inductor; fixed inductor; hybrid control scheme; current stress; DCM; BCM.

I. INTRODUCTION

Compared with the centralized and the string photovoltaic (PV) generation system [1]-[2], PV AC module has been paid more and more attention due to the following advantages: maximum of energy harvest, low cost of mass production, plug

and play operation, easier installation and expansion. The inverter used in AC module is called micro-inverter because of its low power, whose typical value is 100~300W[3]. However, the lower efficiency is the weakness of the micro-inverter compared with the centralized PV generation system, which reduces the competitiveness of the PV AC modules[4]. Thus, the efficiency increasing is an important research field to PV micro-inverter [3], [5].

According to the fact whether there is a transformer in the topology, there are two types of micro-inverters, the transformerless micro-inverter [6]- [8] and the galvanic isolated micro-inverter [9]. The output voltage of a single PV panel is generally about 25~36V at its maximum power point (MPP). Thus, a high step-up prestage DC–DC converter must be equipped to match the grid amplitude voltage in the transformerless micro-inverter, such as 155V (110V RMS) or 311V (220V RMS) [10]. However, the conventional boost or buck/boost cannot have good performance if they have so high step-up. In order to obtain high step-up and good performance, a coupled inductor with large turns-ratio and several power switches are usually employed to help power conversion. The cost and the complexity of this high step-up micro-inverter may not be less than that of the isolated ones. Moreover, some special control strategies or specific poststage DC–AC inverters must be employed to suppress the leakage current [11], which increases complexity of the transformerless micro-inverter.

The commonly used isolated micro-inverter has two stages. The prestage DC–DC converter is usually based on the classical DC/DC converters or their improved topologies, such as flyback[12]-[15], interleaved flyback[16]-[17], forward[18], half-bridge[19], current-fed or voltage-fed push-pull[20]- [21], current-fed isolated dual-boost[22], various kinds of resonant full-bridge[23]-[25]. With the increasing of photoelectric transformation efficiency, the output power of a single PV panel becomes large. The maximum value is beyond 500W in [26]. However, the prevalent two-phase interleaved flyback micro-inverter cannot achieve high efficiency with such high power. High efficiency can be achieved by three or more phase interleaved flyback micro-inverter, which will greatly increase the complexity of the topology. Thus, micro-inverter based on resonant full-bridge has received a lot of attention in recent years due to easier soft-switching, high

efficiency and larger rated power. However, the efficiency of the micro-inverter based on resonant full-bridge is low with light load because of the relatively complex circuit topology.

Some mandatory efficiency standards, such as CEC efficiency and European efficiency [27]- [28], are a weighted value. The PV micro-inverter can obtain a high weighted efficiency only when it always has high efficiency in different solar irradiance and temperature. Many schemes have been proposed for higher weighted efficiency, such as time-sharing strategy for flyback unit in interleaved flyback micro-inverter[29]- [31], variable-frequency (VF) and constant peak current scheme[32], two topologies integrated into a single circuit scheme[33], current boundary continuous mode (BCM) with VF scheme in wide power range[34]-[37].

An adaptive inductor can be used in resonant converter and dual active bridge (DAB) for achieving constant-frequency (CF) control or low circulating energy [38]. However, it hasn't been adopted in micro-inverter in previous work to the best of author's knowledge. In order to meet the power development tendency of a single PV panel, an adaptive inductor is in series with the primary winding of the transformer in full-bridge micro-inverter for achieving current BCM in wide power range with CF. On one hand, high efficiency can be achieved in heavy load due to characteristic of the full-bridge converter. On the other hand, current BCM operation cause low current stress and high efficiency in wide power range.

II. PV MICRO-INVERTER BASED ON FULL-BRIDGE WITH ADAPTIVE INDUCTOR

Fig. 1 shows the proposed topology for PV micro-inverter. It includes a prestage full-bridge DC-DC converter (PFDDC) and a poststage DC-AC inverter (PDAI). PFDDC includes a high-frequency inverter formed by S1-S4, an adaptive inductor L in series with the primary winding of the transformer, the high-frequency transformer, a double-voltage-rectifier formed by D1-D2 and C_1-C_2. The inductance value of the adaptive inductor can be regulated according to the output power of the PV panel for achieving BCM with CF. The operational principle of the adaptive inductor will be discussed in Section III. PDAI is a full-bridge topology modulated by double-frequency unipolar sinusoidal pulse width strategy and it isn't the emphasis of this paper. We focus on the study of PFDDC and its control strategy.

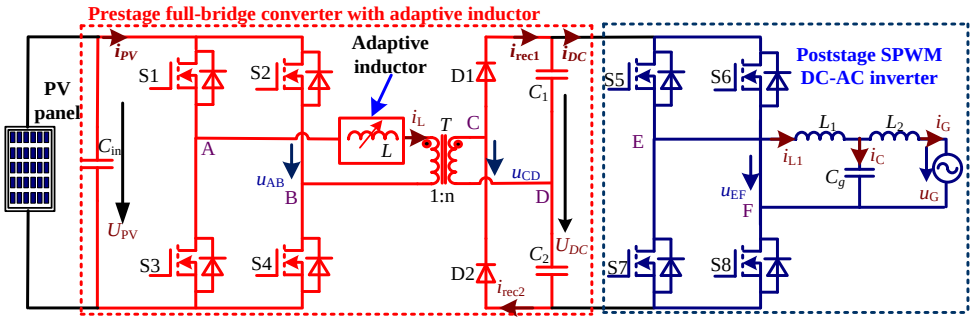

Fig. 1. The proposed topology for PV micro-inverter with adaptive inductor.

The inductance of the adaptive inductor can always be operated in a proper value to guarantee BCM operation within wide power range. Synthetically, the proposed PFDDC with the adaptive inductor for PV micro-inverter has the following characteristics:

1. The adaptive inductor is in series with the transformer and all of switches and diodes are clamped by the filter capacitance with large capacitance. So, there is almost no voltage spike across the rectifier diodes. However, in the conventional full-bridge converter (CFBC), there is voltage spike across rectifier diodes, which results from the resonant process between the leakage inductor, junction capacitor of rectifier diode during the commutation.
2. Compared with the flyback and forward converter, it is easier to achieve high efficiency with high power.
3. There is no energy circulating in PFDDC because there is no feedback current in the input current--that is, the current i_{PV} is always greater than or equal to zero.
4. All of switches and diodes can achieve soft switching through proper modulation.
5. The adaptive inductor can guarantee the current BCM operation and the lowest current stress within wide power range.

Based on the symbols and signal polarities described in Fig. 1, the theoretical waveforms of PFDDC in BCM are shown in Fig. 2. The intervals in Fig. 2 describe the various operational steps of PFDDC during a switching cycle. The operation of the converter is repetitive in a switching cycle. Setting the duty cycle is

$$D = \frac{t_1 - t_0}{0.5(t_8 - t_0)} = \frac{t_1 - t_0}{0.5T_S} \tag{1}$$

Where, T_s is the switching cycle of the converter.

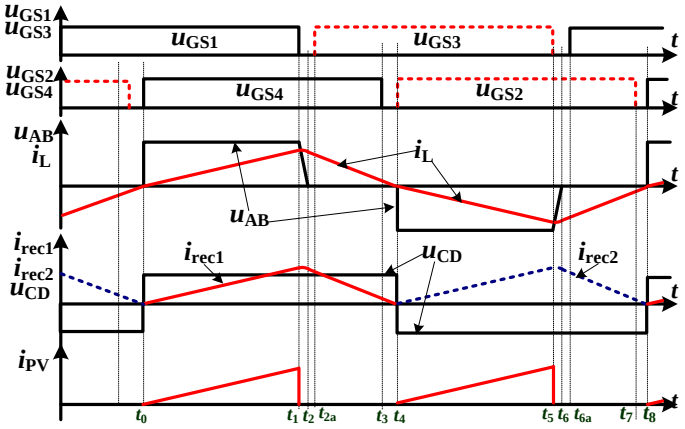

Fig. 2. Theoretical waveforms and switching time of PFDDC. Note that u_{GS1} - u_{GS4} represent drive signal of the corresponding switches, u_{AB} is the output voltage across point A and point B, i_L is the adaptive inductor current, u_{CD} is the output voltage across point C and point D, i_{rec1} and i_{rec2} are the current through rectifier diode D1 and D2 respectively, i_{PV} is input current of PFDDC.

One complete switching cycle can be divided into eight steps. The former four steps are detailedly explained as follows. The operation condition of the later four steps is symmetrical with the former four steps. Fig. 3 gives the commutation step diagrams during half a switching cycle. Note that the parasitic capacitors of switches S1-S4 are considered in Fig. 3.

Step 1: (t_0-t_1, Fig. 3 (a)): The switch S4 is turned on and the voltage u_{AB} is changing from zero to U_{PV} at t_0. The current i_L begins to increase from zero and rectifier diode D1 is ON. The voltage relationship between t_0 to t_1 is as follows:

$$\begin{cases} u_{S1} = u_{S4} = 0 \\ u_{S2} = u_{S3} = U_{PV} \\ u_{AB} = U_{PV} \quad u_{CD} = U_{DC} \quad t \in (t_0, t_1) \\ u_L = U_{PV} - U_{DC}/2n \\ u_{D1} = 0 \quad u_{D2} = U_{DC} \end{cases} \tag{2}$$

Where, u_{S1}-u_{S4} are the voltage across S1-S4, u_L is the voltage across the adaptive inductor L, u_{D1} and u_{D2} are the voltage across the rectifier diode D1 and D2 respectively. According to the voltage relationship in (2), the current expressions are as follows:

$$\begin{cases} i_L = \dfrac{2nU_{PV} - U_{DC}}{2nL}(t - t_1) \\ i_{rec1} = i_L / n \\ i_{rec2} = 0 \\ i_{PV} = i_L \end{cases} \qquad t \in (t_0, t_1) \tag{3}$$

Step 2: (t_1-t_2, Fig. 3 (b)): At t_1, S1 is turned off. The junction capacitance of S1 and S3, together with the adaptive inductor L begin to resonate, which makes voltage across S1 (u_{S1}) increasing from zero and voltage across S3 (u_{S3}) decreasing from the input voltage U_{PV}. So, S1 can achieve zero voltage turn-off. In the secondary side of transformer, the operation condition keeps same with Step 1. The time interval of this step is very short. At t_2, the voltage of each element is as follows:

$$\begin{cases} u_{S1} = u_{S2} = U_{PV} \\ u_{S3} = u_{S4} = 0 \\ u_{AB} = 0 \quad u_{CD} = U_{DC} \\ u_L = -U_{DC} / 2n \\ u_{D1} = 0 \quad u_{D2} = U_{DC} \end{cases} \qquad t = t_2 \tag{4}$$

Step 3: (t_2-t_3, Fig. 3 (c) and Fig. 3(d)): At t_2, body diode of S3 begins to conduct. The voltage of each element in this step is same with the time t_2 shown in Eq. (4) and the current expression is as follows:

$$\begin{cases} i_L = \dfrac{2nU_{PV} - U_{DC}}{nL} DT_S - \dfrac{U_{DC}}{2nL}(t - t_2) \\ i_{rec1} = i_L / n \\ i_{rec2} = 0 \\ i_{PV} = 0 \end{cases} \qquad t \in (t_2, t_3) \tag{5}$$

At t_{2a}, S3 is turned on with ZVS and the operating condition of the converter is the same as that of before t_{2a}. At t_3, the current i_L is falling to zero. According to the volt-second balance of the adaptive inductance L, the duration of this step ($0.5\Delta DT_s$) can be obtained.

$$\Delta D = \frac{t_3 - t_2}{0.5T_S} = \frac{2nU_{PV} - U_{DC}}{U_{DC}} D = 1 - D \tag{6}$$

Step 4: (t_3-t_4, Fig. 3 (e)): At t_3, the current i_L is falling to zero and S4 is turned off at this time. So, S4 can obtain ZCS off. The rectifier diode D1 is off at zero current. Thus, the reverse recovery loss of D1 is very small. There is almost no current

in the circuit in this step and the duration of this step is very short.

At t_4, S2 is turned on, the later four steps begin and the working condition is symmetrical with the former four steps. It is unnecessary to go into details here.

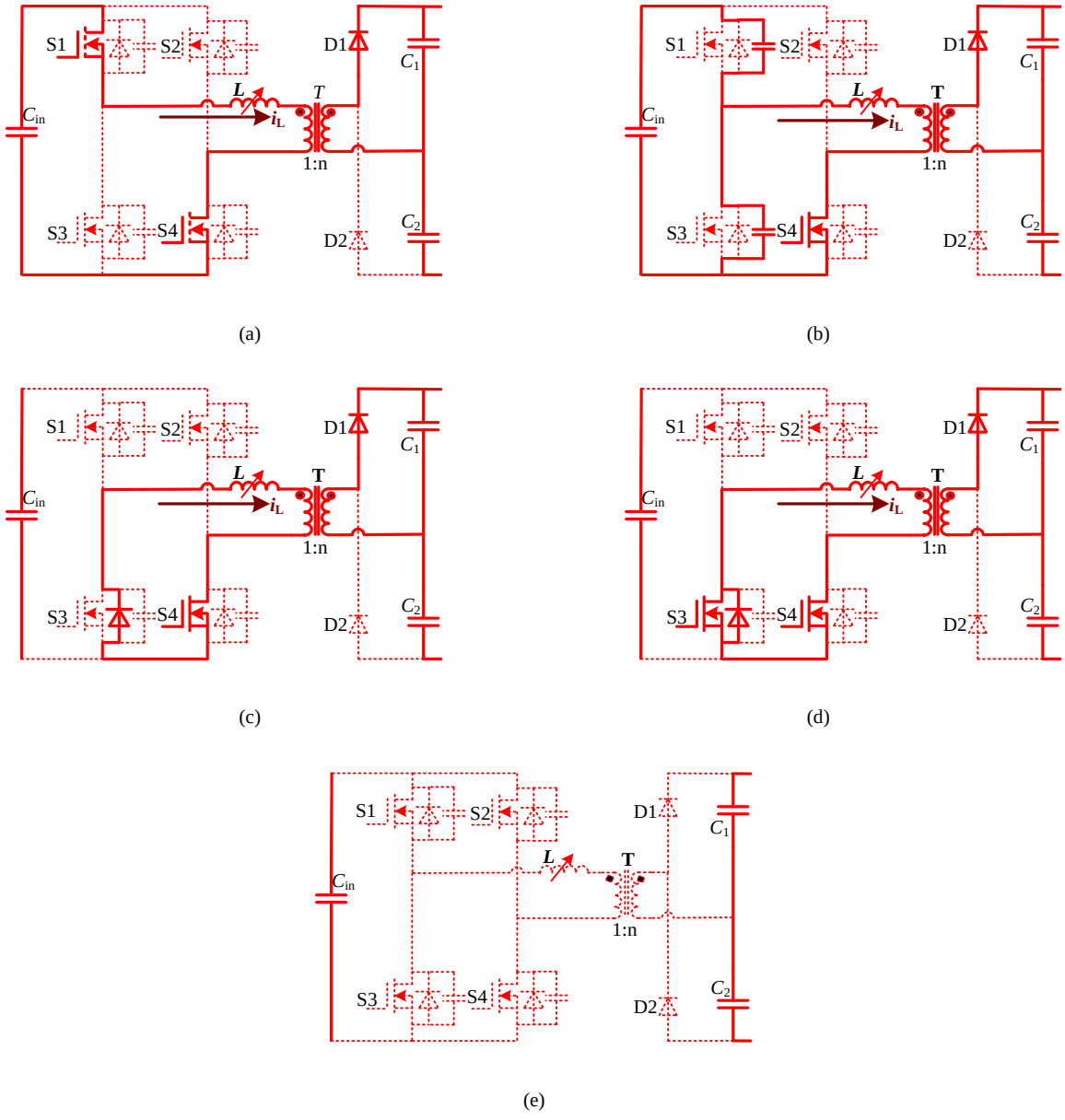

Fig. 3. Commutation step diagrams during half a switching cycle of PFDDC: (a) Step 1: Current path between t_0-t_1, (b) Step2: Current path between t_1-t_2, (c) Step 3: Current path between t_2-t_{2a}, (d) Step 3: Current path between t_{2a}-t_3, (e) Step 4: Current path between t_3-t_4.

III. The Operational Principle of the Adaptive Inductor

The adaptive inductor was built as the structure shown in Fig. 4(a) and its photo is shown in Fig. 4(b), as explained in [39]-[40].

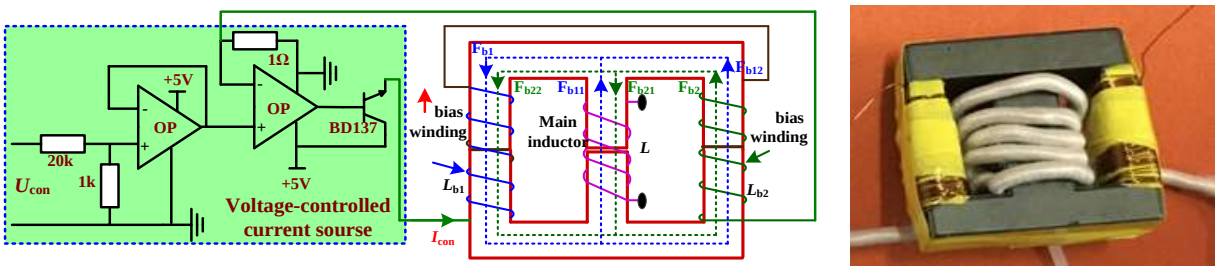

(a) (b)

Fig. 4. Developed adaptive inductor. (a) Schematic diagram. (b) Photograph.

The adaptive inductor *L* is wound around the core center leg (CCL) whereas the symmetrical bias windings L_{b1} and L_{b2} are wound around the core two side arms (CTSA). A bias current I_{con}, which results from a voltage-controlled current source (VCCS), flows through the bias windings L_{b1} and L_{b2}. The magnetomotive forces (MMF) produced by bias windings L_{b1} and L_{b2} are F_{b1} and F_{b2}, respectively. MMF F_{bij} (i=1,2;j=1,2) shown in Fig. 4(a) are the subcomponents of F_{b1} and F_{b2}. The relationship of MMFs produced by bias windings L_{b1} and L_{b2} are

$$\begin{cases} F_{b1} = F_{b11} + F_{b12} \\ F_{b2} = F_{b21} + F_{b22} \\ F_{b1} = F_{b2} \\ F_{b11} = F_{b21} \end{cases} \tag{7}$$

Thus, MMFs F_{b11} and F_{b21} flowing through CCL offset each other and MMF in CCL determines inductance of the adaptive inductor L. The effect of MMF F_{b1} and F_{b12} (or F_{b2} and F_{b21}) with the same direction cause core saturation in CTSA, which can change the effective permeability of CTSA. The effective permeability of CTSA is decreasing with the increasing of the bias current I_{con} and it is equal to 60-70 times of μ_0 (Permeability in a vacuum) with enough bias current I_{con}[39]. At last, the inductance value of the adaptive inductor can be regulated by the bias current I_{con}.

We can divide the core into four parts and the variables of each part are all shown in Fig. 5.

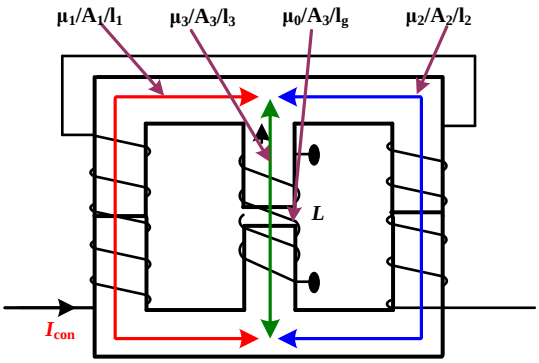

Fig. 5 the magnetic path sections of variable inductor.

With consideration of the leakage inductor L_k, the inductance of the adaptive inductor can be expressed as[39]

$$\frac{1}{L}=[\frac{1}{L_1+L_2+L_k}+\frac{1}{L_3}+\frac{1}{L_g}] \tag{8}$$

Where, $L_1=L_2=\frac{\mu_0\tilde{\mu}A_1n_3^2}{l_1}, L_3=\frac{\mu_0\mu_3A_3n_3^2}{l_3}, L_g=\frac{\mu_0A_3n_3^2}{l_g}, L_k=\frac{16\mu_0A_3n_3^2}{l_3}$. An important variable is the ratio of the maximum inductance to the minimum inductance. Its asymptotic value expression can be derived according to the fact that $\tilde{\mu}_{\max}=\mu_3=\mu_i$ = 2400 (PC40 material) and $\tilde{\mu}_{\min}\approx 65$.

$$\frac{L_{\max}}{L_{\min}}=\frac{1}{16}\frac{l_3}{l_g} \tag{9}$$

The maximum inductance of the adaptive can be achieved through the basic equation of an inductor without consideration of the bias windings.

$$L_{\max}=\frac{\mu_0A_3n_3^2}{l_g} \tag{10}$$

The turns of main winding n3 is

$$n_3=\frac{V_{rms}}{2\Delta B_m f_s A_3} \tag{11}$$

Where V_{rms} is the RMS value of the voltage across the adaptive inductor. Equations (9) and (10) can now be used to obtain an estimate of the core volume needed:

$$V_{core}=A_3(l_1+l_3)=\frac{\mu_0}{L_{\max}}\frac{l_1+l_3}{l_g}\left[\frac{V_{rms}}{2\Delta B_m f_s}\right]^2 \tag{12}$$

According to the parameter of a single PV panel, an approximate fitting line about PV voltage versus output power in a certain temperature is

$$P=55U_{PV}-1630 \quad U_{PV}\in(30,36) \tag{13}$$

The duty cycle in BCM can be determined in terms of (6) in Section II. So,

$$D_{BCM} = \frac{U_{DC}}{2nU_{PV}} \tag{14}$$

The mean value of the input current i_{PV} can be calculated through geometry relationship in Fig. 2.

$$I_{PV} = \frac{(2nU_{PV} - U_{DC})D^2T_S}{8nL} \tag{15}$$

The input-side power is

$$P = U_{PV}I_{PV} = \frac{(2nU_{PV} - U_{DC})U_{PV}D^2T_S}{8nL} \tag{16}$$

If the output power of the converter is P, the inductance value of the adaptive inductor for BCM must equal to

$$L_{BCM} = \frac{(2nU_{PV} - U_{DC})U_{DC}^2T_S}{32n^3PU_{PV}} \tag{17}$$

Fig. 6 shows the L_{BCM} curves varying with different turns ratio of the transformer. It can be seen that L_{BCM} decreases with the increasing of the output power.

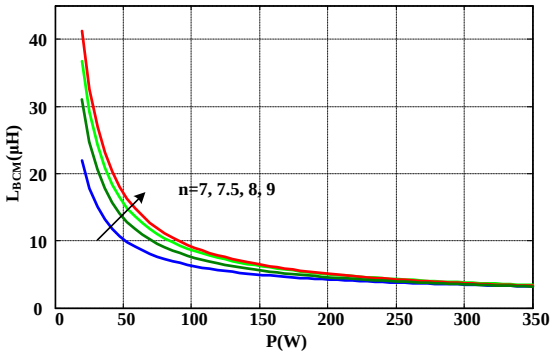

Fig. 6. L_{BCM} curves versus the input power with different turns ratio n.

According to Fig. 6, the needed minimum inductance is 3.3μH. Equation (9) suggests that a large inductance varying range should be required. That is, the air gap (l_g) should be made as small as possible, which may result in saturation of the core. This dictates the use of a rather large air gap to keep the magnetic flux density swing (ΔB_m) small so as to control core losses. Thus, we determine the value of $L_{max}/L_{min} = 5$. With the consideration of characteristic of the adaptive inductor, we select L_{min}=2.5μH and L_{max}=12.5μH. According to the parameters requirement, we selected EE33 (l_1=l_2=0.052m, l_3=0.024m, A_1=A_2=6.1e-5m^2, A_3=1.22e-5m^2) core with material PC40 whose air gap length is 0.3mm. Moreover, the bias windings was implemented by using N_{b1} = N_{b2} = 120 turns with a 0.15mm diameter wire.

In order to satisfy the maximum output power, we select the turns of the adaptive winding n_3=5. So, the maximum inductance of the adaptive inductor is 12.75μH (the actual measured value is 12.4μH) and its inductance curves versus the bias current I_{con} is shown in Fig. 7.

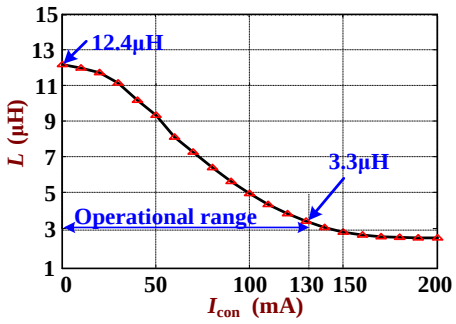

Fig. 7. Inductance curves versus the bias current I_{con}.

It should be noted that the adaptive inductor in [38] is adopted in a resonant converter for achieving soft switching with CF. In this paper, the inductance of the adaptive inductor is regulated in terms of the output power for BCM operation and low current stress with CF. The aims of the adopted adaptive inductor in the two converters are different. It can be seen that the maximum inductance of the adaptive inductor cannot meet the requirement for BCM operation when the power is less than a certain value, which is called the threshold power P_{thr}. So, there are two control schemes for PFDDC of the PV micro-inverter, as shown in Fig. 8. When the power is greater than P_{thr}, the current i_L is in BCM through regulating the inductance of the adaptive inductor in its operational range shown in Fig. 6. When the power is less than P_{thr}, one scheme adopts DCM operation through adjusting duty cycle with maximum inductance of the adaptive inductor. The other scheme adopts BCM operation through adjusting switching frequency also with maximum inductance. This paper adopts Scheme 1 as the final control scheme for easy implementation.

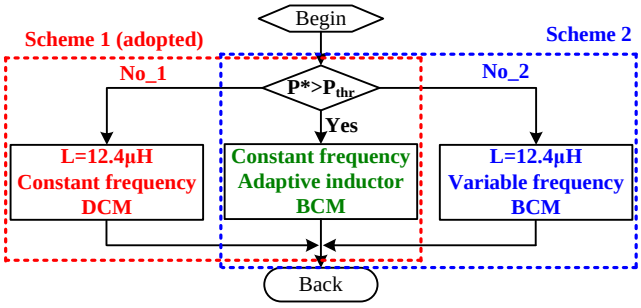

Fig. 8. Two different schemes for PFDDC.

The adaptive inductor is at its maximum inductance 12.4μH and the current i_L is operated in DCM when the power is less than P_{thr}. The duty cycle in DCM can be achieved in terms of (15) and (16). So,

$$D_{DCM} = \sqrt{\frac{8nPL_{\max}}{(2nU_{PV} - U_{DC})U_{PV}T_S}} \tag{18}$$

The core operational condition must be verified. The expected peak value of the flux density for the AC component can be calculated as follows:

$$B_{\max} = \frac{L}{n_3 A_3} i_{L\max} \tag{19}$$

Where, i_{Lmax} is the maximum current of the current i_L and it can be calculated using the duty cycle expression in (14). The curves of B_{max} versus the output power can be achieved from (19), as shown in Fig. 9. It can be seen that the most power range is in BCM zone and the turns ratio (n) can affect the maximum flux density. The larger the turns ratio n is, the bigger the maximum flux density is, which is proportional to the core loss of the transformer. Thus, we expect a smaller turns ratio n from the point of decreasing the core loss. However, the determination of n also needs consideration of other factors, such as conduction loss of switches, etc. We will discuss it in Section V.

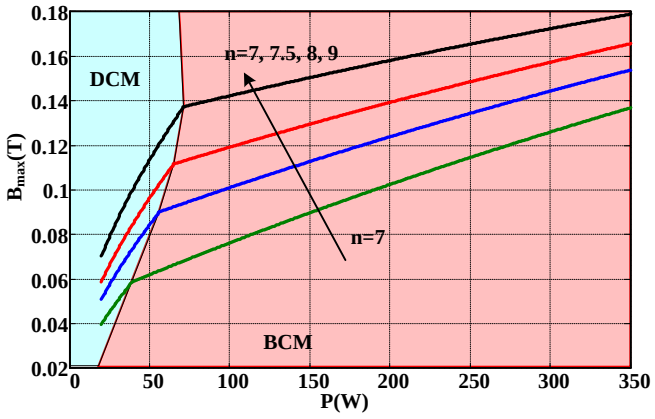

Fig. 9. Curves of B_{max} versus the output power.

IV. The Control Strategy for PFDDC with Adaptive Inductor

The vast majority of the power range is in BCM zone and a fraction of the power range is in DCM zone according to Fig. 9. Therefore, the two operational modes must be distinguished in control strategy. The control strategy diagram for PFDDC

of PV micro-inverter is shown in Fig. 10(a). It is composed of MPPT module, the PV voltage U_{PV} closed-loop, adaptive inductor regulating controller, DCM controller, BCM controller and the mode selector. The control strategy for the poststage SPWM inverter with LCL filter is the same as literature [41] and it won't be discussed here.

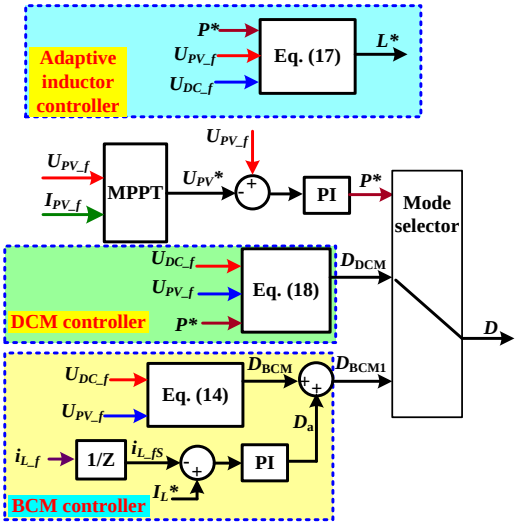

Fig. 10. Control strategy of PFDDC with the adaptive inductor in the PV micro-inverter.

A. control strategy for BCM with adaptive inductor

The duty cycle in BCM is only related to the ratio of the voltage U_{DC} over the voltage U_{PV} and it has nothing to do with the power P dealt by the converter in terms of (14). So, we can regulate the proper inductance of the adaptive inductor according to (17).

The adopted duty cycle in BCM D_{BCM1} includes two components. One is D_{BCM} determined by (10) and the other one D_a results from the adaptive current closed-loop regulator for lower loss in the process of switching. So, $D_{BCM1}=D_{BCM}+D_a$. In Fig. 2, if the current i_L at t_3 is zero, the voltage across S4 u_{S4} is equal to zero and the voltage across S2 u_{S2} is equal to U_{PV} before S2 is turned on at t_4. Thus, the energy stored in parasitic capacitor of S2 (or an external capacitor is paralleled with the switch) will waste at t_4 and the electromagnetic interference will happen. In order to remove this power loss, the current i_L at t_3 (or t_7) is detected as i_{L_fs} in Fig. 11 and setting its reference I_L* is greater (or less) than and near zero. The smaller I_L* doesn't affect the RMS value of i_L much. The waveforms are shown in Fig. 11(a) by adopting the adaptive current closed-loop. It can be seen that the u_{S2} and u_{S4} are always equal zero at its turn-on time if the detecting point x (y) of i_L is

greater (less) than zero. Thus, there is no energy loss in S2 and S4 when they are turned on. Fig. 11(b) shows simulation waveforms of PFDDC after adopting the adaptive current closed-loop and its I_L*=2A.

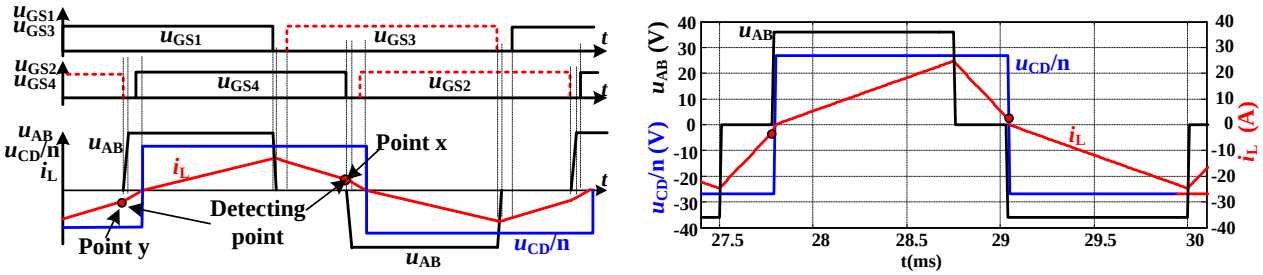

Fig. 11. The waveforms of PFDDC after adopting the adaptive current closed-loop: (a). theoretical waveforms, (b). Simulink waveforms.

B. control strategy in DCM with adaptive inductor

The duty cycle in DCM is not only related to the voltage U_{DC} and U_{PV}, but also related to the power P. The advantage in DCM is the simple control because the inductance of the adaptive inductor is always in its maximum value. The voltage-controlled current source I_{con} is always equal to zero.

In the conventional control strategy, the output signal of the PV voltage closed-loop is as the reference value of the current loop. The output signal of the PV voltage closed-loop is the power reference value in this paper. The duty cycle can be obtained according to the mathematical model in Section III, which can improve the dynamic performance of the converter. There may be some errors between the reference P* and the actual power P. However, it cannot affect the operation of the converter because the PV voltage closed-loop can always output a proper reference power to guarantee the power balance of the PV-side and the grid-side.

V. COMPARISON WITH DIFFERENT SCHEMES

A. Circuit Configuration Comparison with other PV micro-inverter

The circuit configuration of the full-bridge PV micro-inverter shown in Fig. 1 is actually a little more complex than the conventional micro-inverter based on a single flyback converter. However, its efficiency is higher. Moreover, its configuration is even simple compared with to other PV micro-inverters listed in Table I. The contents of comparison include the number and the peak voltage of switches and diodes, clamping circuit, spike voltage, feedback current,

switching frequency and reported maximum efficiency.

TABLE I

PERFORMANCE COMPARISON OF DIFFERENT MICRO-INVERTER

Micro-inverter	Prestage converter		Poststage inverter	Clamping circuit	Spike due to leakage inductor	Feedback current	Switching frequency	Reported maximum efficiency
	Peak voltage		Peak voltage					
Micro-inverter based on a single flyback in [12]	SW (1)	D_{Fly} (1)	S_1- S_4 (4)	RCD snubber	Medium	**No**	**Constant**	90%
	$U_{PV}+\sqrt{2}U_G/n$	$nU_{PV}+\sqrt{2}U_G$	$\sqrt{2}U_G$					
Interleaved flyback micro-inverter in [31]	S_1- S_2 (2)	D_1- D_2 (2)	S_3- S_6 (4)	**No**	Large	**No**	**Constant**	94.1%
	$U_{PV}+\sqrt{2}U_G/n$	$nU_{PV}+\sqrt{2}U_G$	$\sqrt{2}U_G$					
Interleaved flyback micro-inverters with active clamping circuit in [35]	S_1- S_2 (2)	D_1- D_2 (2)	S_3- S_6 (4)	2 switches 2 capacitors	**Small**	**No**	Variable	95.8%
	$U_{PV}+\sqrt{2}U_G/n$	$nU_{PV}+\sqrt{2}U_G$	$\sqrt{2}U_G$					
micro-inverter based on current-fed push-pull converter in [26]	S_1- S_2 (2)	D_1- D_2 (2)	S_3- S_6 (4)	**No**	Large	**No**	**Constant**	93.8%
	U_{DC}/n	U_{DC}	U_{DC}					
micro-inverter based on current-fed push-pull converter with resonant unit in [21]	S_1- S_2 (2)	D_1- D_2 (2)	S_3- S_6 (4)	**No**	Large	**No**	Variable	96.5%
	U_{DC}/n	U_{DC}	U_{DC}					
micro-inverter based on Boost-Half-Bridge in [19]	S_1- S_2 (2)	D_1- D_2 (2)	S_3- S_6 (4)	**No**	Medium	small	**Constant**	98.1%
	$U_{C1}+U_{C2}$	U_{DC}	U_{DC}					
micro-inverter based on full-Bridge cycloconverter in [25]	S_1- S_4 (4)	--	S_5- S_{12}(8)	2 switches 2 inductors 4 diodes	**Small**	**No**	**Constant**	96%
	U_{PV}	--	U_{DC}					
micro-inverter in this paper	S_1- S_4 (4)	D_1- D_2 (2)	S_5- S_8 (4)	**No**	**Almost no**	**No**	**Constant**	93.6%
	U_{PV}	U_{DC}	U_{DC}					

The number of switches and diodes in the proposed micro-inverter is ten and it is not the largest one. The micro-inverter based on the full-Bridge cycloconverter in [25] has twelve switches. The other micro-inverters have fewer switches and diodes compared with the proposed one. However, they are all sustained spike voltage caused by the leakage inductor of the transformer except for the boost-half-bridge micro-inverter in [19]. Thus, clamping circuit is employed to suppress this spike voltage, which results in increasing of switches number. There is feedback current in the boost-half-bridge micro-inverter and there is no feedback current in the other micro-inverters, including the proposed micro-inverter. It can be seen that each performance of the proposed micro-inverter is better than others from the factors listed in Tab. I.

According to the given efficiency in the corresponding literature, the maximum efficiency of the proposed converter is not the highest one. The efficiency of a converter is not only related to the topology itself but also related to many factors, such as device selection, manufacturing process of the inductor and transformer, etc.

B. Comparison between VF_BCM and CF_BCM

In order to achieve high efficiency, switching frequency in some micro-inverters is variable in Tab. I. If the inductance is fixed, the switching frequency must be variable for BCM operation (VF_BCM) and its value can be achieved from (16).

$$f_S = \frac{(2nU_{PV} - U_{DC})U_{PV}D_{BCM}^2}{8nLP} \tag{20}$$

Where, f_s is the switching frequency of switches in PFDDC. Its curve varying with power is shown in Fig. 12 with the data in Section VI. The lower the output power is, the higher switching frequency it needed. High frequency operation may cause many adverse effects, such as higher drive loss and magnetic loss in the transformer and inductor, parasitic parameters and dead-time effect, etc.

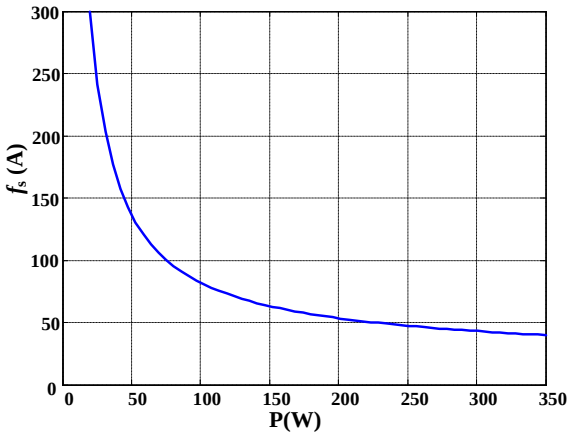

Fig. 12. Switching frequency versus output power under VF BCM.

PFDDC can be operated in CF_BCM in wide power range with an adaptive inductor, as shown in Fig. 9. The price of the CF_BCM is that there is a little power loss in VCCS, whose typical value is from 0 to 0.65W according to Fig. 7. When the output power is low, the needed inductance should be large and the loss in VCCS is approximately zero. When the output power is at its rated value, the loss is 0.65W and it only accounts for 0.18% of the rated power. Moreover, the cost of the VCCS is low because the used elements in Fig. 4(a) are cheap.

The RMS value of the current i_L is same at different modes mentioned above and its value is shown in the following subsection.

C. Comparison between DCM and CF_BCM

The most convenient method for CF operation is regulating duty cycle to realize DCM. The RMS current through S1-S4 is always equal to $(1/\sqrt{2})$ times of the RMS value of current i_L. So, we will analyze the value of i_L.

Current stress analysis with the adaptive inductor (CF_BCM**)**

As shown in Figs. 7 and 9, the current i_L is in BCM when the power is greater than P_{thr} and the current i_L is in DCM when the power is less than P_{thr}. So, the RMS current value must be calculated in stages.

The peak value of the current i_L in BCM or DCM is

$$i_{L\_pk} = \frac{(2nU_{PV} - U_{DC})}{4nL} DT_S \tag{21}$$

According to the geometry relationship in Fig. 2, we can achieve the RMS value expression of i_L in BCM and substitute (21) into it. Then

$$I_{L\_BCM} = \frac{\sqrt{3}}{3} i_{L\_pk} = \frac{4\sqrt{3}nP}{3U_{DC}} \quad (P > P_{thr}) \tag{22}$$

It can be seen that the smaller turns ratio n is, the RMS value of i_L is lower. The threshold power P_{thr} can be achieved from (17) when the adaptive inductance in its maximum value (L_{max}=12.4μH in this paper).

In DCM with the adaptive inductor, the duty cycle is shown in (17) and the duty cycle for current decreasing is

$$\Delta D = \frac{(2nU_{PV} - U_{DC})}{U_{DC}} D_{DCM} \tag{23}$$

Similarly, the RMS value expression of i_L in DCM with the adaptive inductor can be calculated.

$$I_{L\_DCM} = \frac{(2nU_{PV} - U_{DC})}{4nL_{\max}} D_{DCM} \sqrt{\frac{D_{DCM} + \Delta D}{3}} T_S \tag{24}$$

Current stress analysis with a fixed inductor (DCM**)**

In the conventional converter, such as dual active bridge (DAB), a fixed inductor is in series with the primary winding of

the transformer. The inductance of the fixed inductor can be determined from (17) when $P=P_{max}$. So

$$L_{fix}=\frac{(2nU_{PV\_max}-U_{DC})U_{DC}^2T_S}{32n^3(55U_{PV\_max}-1630)U_{PV\_max}} \tag{25}$$

The current i_L is in DCM in the whole power range if the fixed inductor is used in terms of (25). The RMS value expression of i_L with the fixed inductor can be achieved

$$I_{L\_fix}=\frac{(2nU_{PV}-U_{DC})}{4nL_{fix}}D_{fix}\sqrt{\frac{D_{fix}+\Delta D_{fix}}{3}}T_S \tag{26}$$

Where, $D_{fix}=\sqrt{\frac{8nPL_{fix}}{(2nU_{PV}-U_{DC})U_{PV}T_S}}$, $\Delta D_{fix}=\frac{(2nU_{PV}-U_{DC})}{U_{DC}}D_{fix}$.

The current stress curves are achieved from (22), (24) and (26) with different turns ratio n, as shown in Fig. 13. With the same turns ratio, the current stress under the adaptive inductor is always less than that of under the fixed inductor. Thus, PFDDC with the adaptive inductor should be a better choice for decreasing the conduction loss of the switches and copper loss of the transformer. The current stress will rise with the increasing of turns ratio n. Theoretically, if $n>(U_{DC}/2U_{PV})$, a proper inductance can always be found to guarantee the maximum output power. The smaller turns ratio n it is, the lower inductance is. On one hand, there is leakage inductance of the transformer. On the other hand, the inductance range of the adaptive cannot reach too low. At last, we select n=7.5.

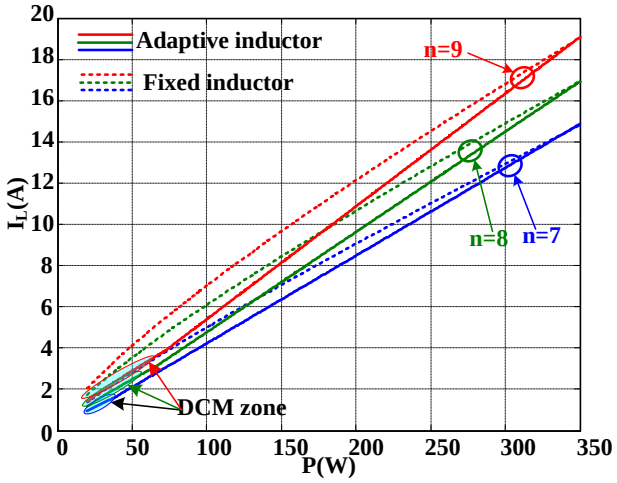

Fig. 13. Comparison with current stress between adaptive inductor and fixed inductor with different turns ratio.

D. Loss comparison between DCM, VF_BCM and CF_BCM operational modes

The power loss mainly includes conduction loss P_{con}, switching loss P_{sw}, core loss P_{core}, copper loss P_{cu} and dive loss P_{dr} in PFDDC. The conduction loss includes loss from four Mosfets and two diodes.

$$P_{con}=\begin{cases}2R_{on}I_{L\_fix}^2+2V_FI_D & \text{DCM}\\ 2R_{on}I_{L\_BCM}^2+2V_FI_D & \text{VF BCM}\\ 2R_{on}I_{L\_BCM}^2+2V_FI_D & \text{CF BCM}\end{cases} \tag{27}$$

Where, R_{on} is the conduction resistance of the switches S1-S4, V_F is voltage drop of the diode D1-D2 and I_D is the mean value of the current of diodes D1-D2.

All of the switches and diodes can achieve ZCS or ZVS. In stability state, the output power and the output voltage of the PV panel is constant. Thus, the inductance of the adaptive inductor is constant and the condition of ZVS operation is similar with that of the fixed inductor. In the dynamic process, the inductance of the adaptive inductor is in the stated range shown in Fig. 7 (3.3μH-12.4μH). The stored energy in the adaptive inductor cannot change abruptly. Thus, ZVS operation can also be realized. However, the energy stored in parasitic capacitor of S2 or S4 will waste if a proper scheme will not be used. So, we adopt the scheme in Fig. 10 to overcome this shortcoming. The scheme in Fig. 10 can only be used in VF_BCM and CF_BCM. As a result, the wasted energy only occurs in DCM scheme.

$$P_{sw}=\begin{cases}C_{oss}U_{PV}^2f_s & \text{DCM}\\ 0 & \text{VF BCM}\\ 0 & \text{CF BCM}\end{cases} \tag{28}$$

Where C_{oss} is the equivalent capacitance of the parasitic capacitor of switch and the external paralleled capacitor.

The core loss of the transformer and the inductor can be estimated in terms of Steinmetz equation [42].

$$P_{core}=kf_s^{\alpha}B_{peak}^{\beta} \tag{29}$$

Where, f_s is the switching frequency, B_{peak} is the peak magnetic flux density, k, α, β are the Steinmetz coefficient determined by the core material.

The copper loss not only includes the loss from the windings of the transformer and the inductor, but also includes the loss from line resistance and its expression is

$$P_{cu}=\begin{cases} R_x I_{L\_fix}^2 & \text{DCM} \\ R_x I_{L\_BCM}^2 & \text{VF BCM} \\ R_x I_{L\_BCM}^2 & \text{CF BCM} \end{cases} \tag{30}$$

Where, R_x is lumped resistance of the transformer windings, inductor windings and circuit line referred to primary side.

The drive loss is proportional to switching frequency because the energy loss in every on-off process is same.

$$P_{dr}=4f_s(Q_{on}+Q_{off}) \tag{31}$$

Where Q_{on} and Q_{off} are the wasted energy in every turning-on process and the turning-off process of switches.

The bar diagram of the loss with different output power is shown in Fig. 14 according to Eqs. (27)-(31). The loss under CF_BCM is the lowest in the whole output power range and it is approximately equal to the loss under VF_BCM at its rated output power. So, the weighted efficiency of the CF_BCM scheme in this paper is the highest among the three control schemes analyzed above.

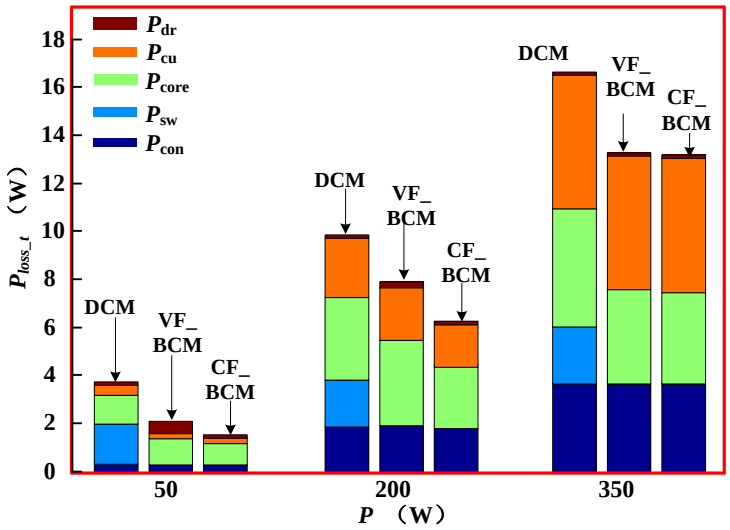

Fig. 14. Loss comparison with different operational modes.

VI. Experimental Verification

In order to verify feasibility of the proposed PFDDC with the adaptive inductor for PV micro-inverter, a 350W PV micro-inverter prototype was built. The parameters and elements model are shown in Table II.

Fig. 15 shows operational waveforms of PFDDC in steady state with the adaptive inductor when the output power is 350W. The waveforms of the voltage u_{AB}, the current i_L, and the drive voltage u_{GS4} and terminal voltage $u_{S4}$of switch S4 in

lagging leg is shown in Fig. 15 (a). The turn-on time and turn-off time always happen at i_L=0 and the conduction interval coincides with the positive of i_L. Thus, S4 achieves ZCS turn-on and turn-off. The other switch S2 in lagging leg has the same characteristic with the switch S4. The waveforms of the voltage u_{AB}, the current i_L, and the drive voltage u_{GS1} and terminal voltage $u_{S1}$of switch S1 in the leading leg are shown in Fig. 15 (b) and Figs. 15 (c)-(d) are the zoomed waveforms of turn-on process and turn-off process of S1. It can be seen that the voltage has dropped to zero before turn-on time of S1. So, S1 achieves ZVS turn-on. The rising time of terminal voltage u_{S1} is 0.2μs after its driven voltage u_{GS1} becomes zero and this duration can absolutely guarantee its turn-off. Therefore, S1 also realizes ZVS turn-off. The other switch S3 in the leading leg has the same characteristic with the switch S1.

TABLE II

PARAMETERS AND ELEMENTS MODEL FOR MICRO-INVERTER PROTOTYPE

Switching frequency	Prestage DC/DC:40kHz Poststage DC/AC: 10kHz
Grid voltage	$220\sqrt{2}\sin(100\pi t)$
PV panel	Maximum power：350W Voltage in MPP：36V
Switches	S1-S4: IRFB4110 D1-D2:C3D05060A S5-S8:C2M0080120D
Filter capacitors	C_{in}:200μF/50V C_1, C_2:470μF/250V C_f:10μF/250V
Inductors	L:3.3-12.4μH(adaptive inductor) L:3.3 μH(fixed inductor) L_1:1mH L_2:0.5mH
Transformer	n=7.5

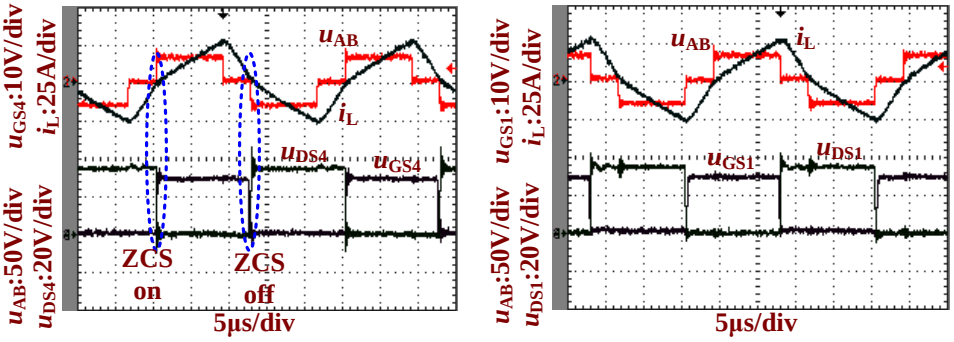

(a) (b)

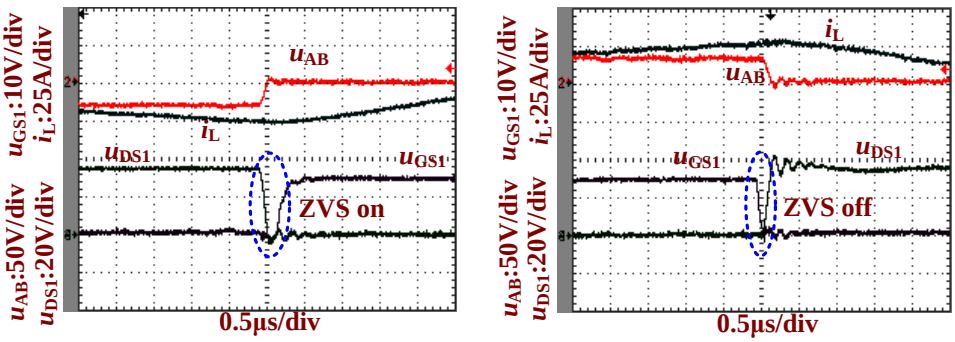

(c) (d)

Fig. 15. The waveforms of PFDDC with the adaptive inductor: (a) waveforms of u_{GS4}, u_{S4},i_L and u_{AB}, (b) waveforms of u_{GS1}, u_{S1},i_L and u_{AB}, (c) zoomed waveforms of turn-on process of S1, (d) zoomed waveforms of turn-off process of S1.

Fig. 16 shows the control effect comparison between the adaptive inductor and the fixed inductor under conditions of 350W, 200W, 100W and 30W, respectively. The given waveforms include u_{AB}, i_L, the secondary voltage of the transformer u_{CD}, and the reverse voltage of the rectifier diode D2 u_{D2}. From the waveforms with the adaptive inductor shown in Figs. 16(a) - (d), the reverse recovery loss can be effectively decreased because the commutation form D1 to D2, or vice versa, always occurs at zero current. Moreover, the current i_L is in BCM in wide power range, which can effectively decrease the current stress and improve the efficiency of the converter. The duty cycle is a larger value (comparison with the fixed inductor scheme shown in Fig.16(h)) even if the output power is 30W shown in Fig.16(d). This characteristic guarantee that the rising slope of i_L is smaller and lower current stress.

Figs. 16(e)-(h) show the waveforms with the fixed inductor and its inductance value is 12.4μH. The current i_L is operated in DCM except for full load and its peak value is higher than that of the peak current under the adaptive inductor condition.

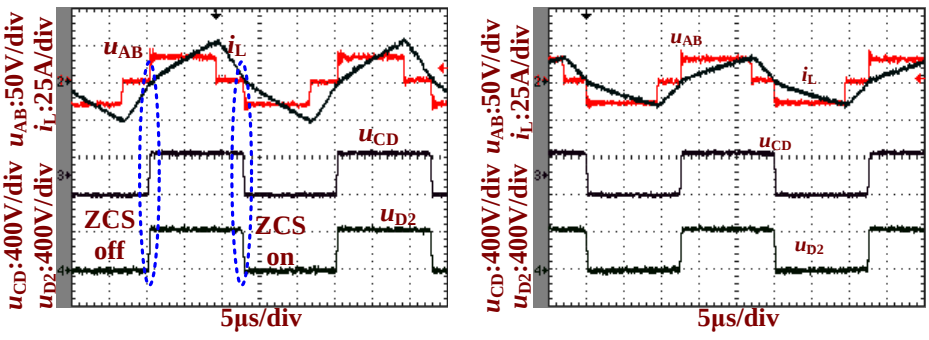

(a) (b)

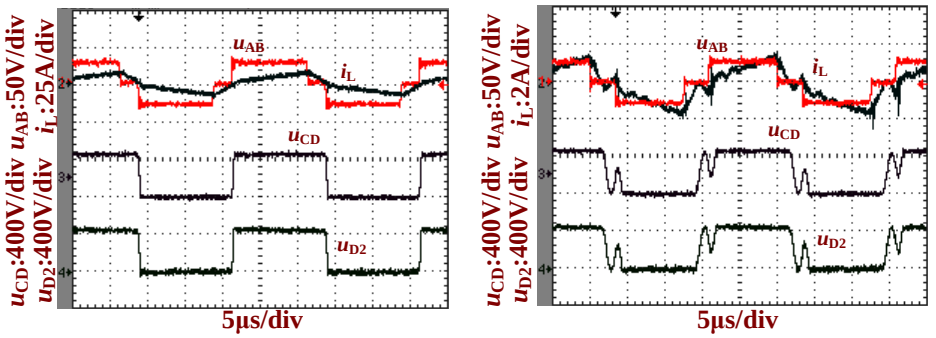

(c)

(d)

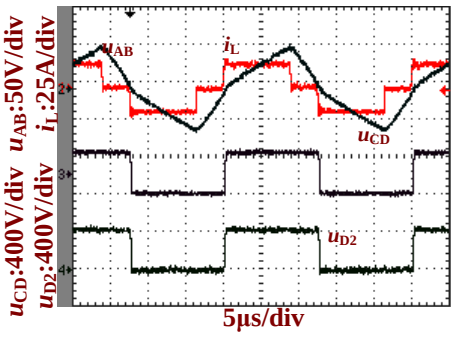

(e)

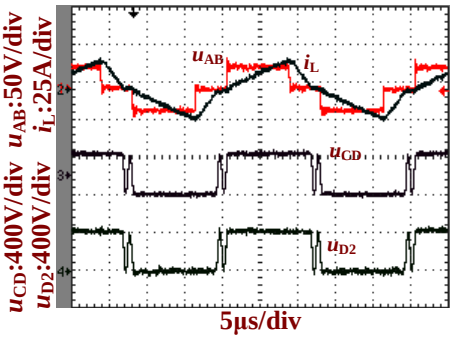

(f)

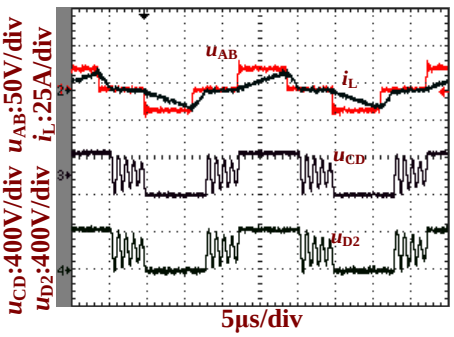

(g)

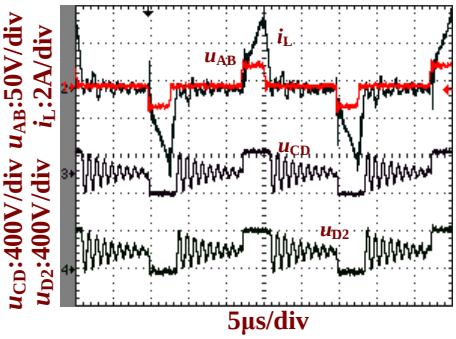

(h)

Fig. 16. The waveforms of the PFDDC with the adaptive inductor and fixed inductor: (a) P=350W with the adaptive inductor, (b) P=200W with the adaptive inductor, (c) P=100W with the adaptive inductor, (d) P=30W with the adaptive inductor, (e) P=350W with the fixed inductor, (f) P=200W with the fixed inductor, (g) P=100W with the fixed inductor, (h) P=30W with the fixed inductor.

Fig. 17 shows the waveforms of the micro-inverter when the PV power has a sudden change. The waveforms of the voltage u_{AB} and the current i_L are shown in Figs. 17(a) and (b) when the PV power has a sudden-decrease and sudden-increase, respectively. The DC bus voltage U_{DC} cannot be changed much due to the large capacitance of C_1-C_2 when PV power has a sudden change. So, the inductance of the adaptive inductor should be adjusted and the duty cycle holds constant, which can guarantee the power balance in filter capacitor C_{in}. The waveforms of voltage U_{DC} and the current i_G are

shown in Figs. 17(c) and (d) when the PV power has a sudden-decrease and sudden-increase, respectively. The amplitude of the grid current reference I_G* is obtained from the DC bus voltage U_{DC} closed-loop regulator according to the control scheme of the poststage DC/AC inverter in Fig. 10(b). The larger capacitance of DC bus filter capacitors C_1 and C_2 determines the changing speed of the DC voltage U_{DC} is slow. Thus, the amplitude of grid current i_G increases or decreases gradually. At last, the dynamic process for DC bus voltage U_{DC} regulator needs a long time, as shown in Figs. 17(c) and (d).

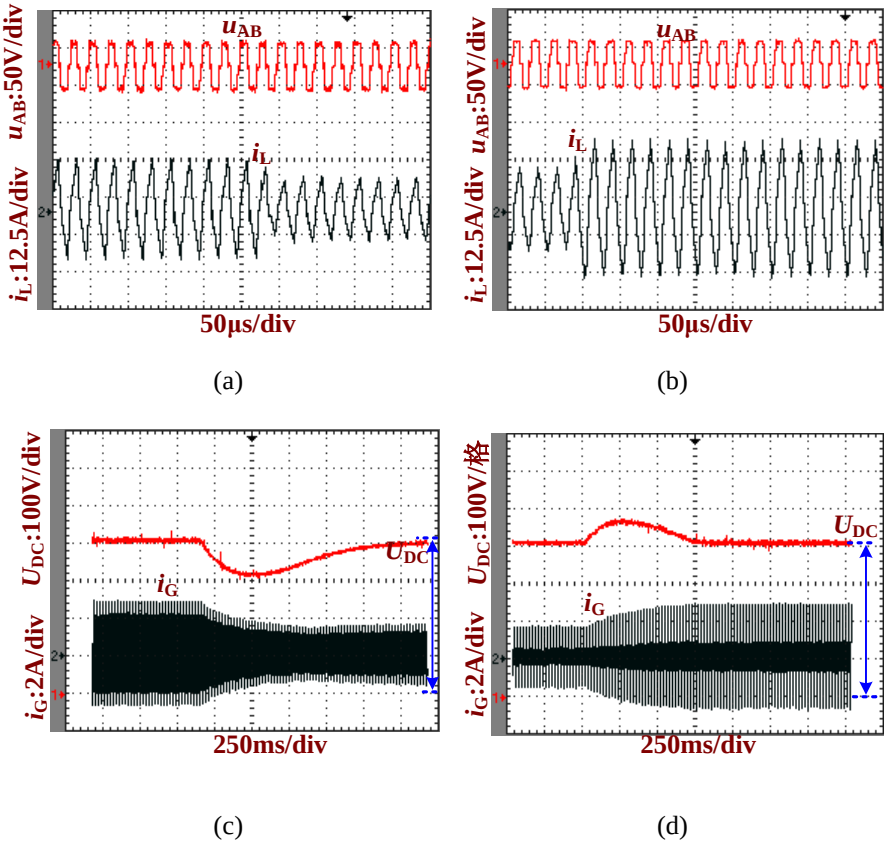

Fig. 17. The dynamic waveforms of the micro-inverter: (a) the voltage u_{AB} and the current i_L with a suddenly-decreased PV power, (b) the voltage u_{AB} and the current i_L with a suddenly-increased PV power, (c) the voltage U_{DC} and the grid current i_G with a suddenly-decreased PV power, (d) the voltage U_{DC} and the grid current i_G with a suddenly-increased PV power.

Fig. 18 shows the total efficiency curve of the PV micro-inverter, the sub-efficiency curve of PFDDC and the sub-efficiency curve of the postsage DC/AC inverter with the adaptive inductor or the fixed inductor. When the output power is near the full-load, the efficiency of the proposed scheme is a little lower than that of the conventionally fixed inductor because there is energy loss for driving magnetic bias windings. While the output power is lower than 300W, the efficiency of the proposed scheme is obviously higher than that of the fixed inductor scheme.

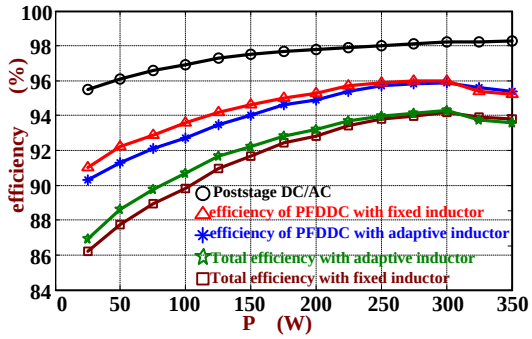

Fig. 18. Efficiency curves of the micro-inverter with adaptive inductor and the fixed inductor.

VII. CONCLUSION

This paper proposes a PFDDC with an adaptive inductor for PV micro-inverter. The inductance of the adaptive inductor can be properly regulated according to the output power and the input and output voltage, which can guarantee that the current is in BCM in wide power range and the current stress of the switches can be deceased obviously. The inductance of the adaptive inductor has an operational range. So, the current is in DCM when the power is lower than the threshold value. A hybrid control strategy, which includes the adaptive inductor adjusting, DCM and BCM schemes in different power range, is proposed after synthesizing these characteristic. The current stress of switch in PFDDC with the adaptive inductor is less than that of switch in PFDDC with the fixed inductor. Thus, the efficiency is the highest one compared with the conditions of VF_BCM and the fixed indctor. The experimental results show that the correctness of the theoretical analysis.

REFERENCES

[1] C. A. Rojas, M. Aguirre, S. Kouro, T. Geyer and E. Gutierrez, "Leakage Current Mitigation in Photovoltaic String Inverter Using Predictive Control With Fixed Average Switching Frequency," *IEEE Trans. Ind. Electron.*, vol. 64, no. 12, pp. 9344–9354, Dec. 2017.

[2] F. Wu, X. Li, F. Feng, and H. B. Gooi, "Multi-topology-mode grid-connected inverter to improve comprehensive performance of renewable energy source generation system," IEEE Trans. Power Electron., vol. 32, no. 5, pp. 3623-3633, May 2017.

[3] Q. Li and P.Wolfs, "A review of the single phase photovoltaic module integrated converter topologies with three different DC link configurations," *IEEE Trans. Power Electron.*, vol. 23, no. 3, pp. 1320–1333, May 2008.

[4] Y. Zhou, L. Liu, and Hui Li, "A High-Performance Photovoltaic Module-Integrated Converter (MIC) Based on Cascaded Quasi-Z-Source Inverters (qZSI) Using eGaN FETs," IEEE Trans. Power Electron., vol. 28, no. 6, pp. 2727–2738, Jun. 2013.

[5] S. B. Kjaer, J. K. Pedersen, and F. Blaabjerg, "A Review of Single-Phase Grid-Connected Inverters for Photovoltaic Modules," IEEE Trans. Ind.

Appl., vol. 41, no. 5, pp. 1292–1306, Sep./Oct. 2005.

[6] D. Meneses, F. Blaabjerg, O.Garcia, and J. A. Cobos, “Review and Comparison of Step-Up Transformerless Topologies for Photovoltaic AC-Module Application,” IEEE Trans. Power Electron., vol. 28, no. 6, pp. 2649–2663, Jun. 2013.

[7] F. C. Melo, L. S. Garcia, L. C. de Freitas, E. A. A. Coelho, V. J. Farias, and L. C. G. de Freitas, “Proposal of a Photovoltaic AC-Module With a Single-Stage Transformerless Grid-Connected Boost Microinverter,” IEEE Trans. Ind. Electron., vol. 65, no. 3, pp. 2289–2301, Mar. 2018.

[8] R. Wai, C. Lin, C. Lin, R. Duan, and Y. Chang, “High-Efficiency Power Conversion System forKilowatt-Level Stand-Alone Generation Unit With Low Input Voltage,” IEEE Trans. Ind. Electron., vol. 55, no. 10, pp. 3702–3714, Oct. 2008.

[9] F. Evran, “Plug-in repetitive control of single-phase grid-connected inverter for AC module applications,” IET Power Electron., vol. 10, no. 1, pp. 47–58, Jan. 2017.

[10] S. A. Arshadi, B. Poorali, E. Adib, and H. Farzanehfard, “High Step-Up DC–AC Inverter Suitable for AC Module Applications,” IEEE Trans. Ind. Electron., vol. 63, no. 2, pp. 832–839 Feb. 2016.

[11] W. Yu, J. Lai, H. Qian, and C. Hutchens, “High-Efficiency MOSFET Inverter with H6-Type Configuration for Photovoltaic Nonisolated AC-Module Applications,” IEEE Trans. Power Electron., vol. 26, no. 4, pp. 1253–1260, Apr. 2011.

[12] S. Zengin, F. Deveci, M. Boztepe, “Volt-second-based control method for discontinuous conduction mode flyback micro-inverters to improve total harmonic distortion,” IET Power Electron., vol. 8, no. 4, pp. 1600–1607, Aug. 2013.

[13] S. Ozturk, and I. Cadirci,, “A Generalized and Flexible Control Scheme for Photovoltaic Grid-Tie Microinverters,” IEEE Trans. Ind. Appl., vol. 54, no. 1, pp. 505–516, Jan./Feb. 2018.

[14] D. Hamza, M. Qiu, and P. K. Jai, “Application and Stability Analysis of a Novel Digital Active EMI Filter Used in a Grid-Tied PV Microinverter Module,” IEEE Trans. Power Electron., vol. 28, no. 6, pp. 2867–2874, Jun. 2013.

[15] T. Shimizu, K. Wada, and N. Nakamura, “Flyback-Type Single-Phase Utility Interactive Inverter With Power Pulsation Decoupling on the DC Input for an AC Photovoltaic Module System,” IEEE Trans. Power Electron., vol. 21, no. 5, pp. 1264–1272, May. 2006.

[16] Z. Zhang, M. Chen, W. Chen, C. Jiang, and Z. Qian, “Analysis and Implementation of Phase Synchronization Control Strategies for BCM Interleaved Flyback Microinverters,” IEEE Trans. Power Electron., vol. 29, no. 11, pp. 5921–5932, Nov. 2014.

[17] F. F. Edwin, W. Xiao, and V. Khadkikar, “Dynamic Modeling and Control of Interleaved Flyback Module-Integrated Converter for PV Power Applications,” IEEE Trans. Ind. Electron., vol. 61, no. 3, pp. 1377–1388, Mar. 2014.

[18] D. Meneses, O. Garcia, P. Alou, J. A. Oliver, and J. A. Cobos, “Grid-Connected Forward Microinverter With Primary-Parallel Secondary-Series Transformer,” IEEE Trans. Power Electron., vol. 30, no. 9, pp. 4819–4830, Sep. 2015.

[19] S. Jiang, D. Cao, Y. Li, and F. Peng, “Grid-Connected Boost-Half-Bridge Photovoltaic Microinverter System Using Repetitive Current Control and Maximum Power Point Tracking,” IEEE Trans. Power Electron., vol. 27, no. 11, pp. 2711–2722, Nov. 2012.

[20] C. T. Rodr ́guez, D. V. Fuente, G. Garcera, E. Figueres, and J. A. G. Moreno, “Reconfigurable Control Scheme for a PV Microinverter Working in

Both Grid-Connected and Island Modes," IEEE Trans. Ind. Electron., vol. 60, no. 4, pp. 1582–21595, Apr. 2013.

[21] Y. Kim, S. Shin, J. Lee, Y. Jung, and C. Won, "Soft-Switching Current-Fed Push–Pull Converter for 250-W AC Module Applications," IEEE Trans. Power Electron., vol. 29, no. 2, pp. 863–872, Feb. 2014.

[22] H. Chiu, Y. Lo, C. Yang, S. Cheng, C. Huang, C. Chuang, M. Kuo, Y. Huang, Y. Jean, and Y. Huang, "A Module-Integrated Isolated Solar Microinverter," IEEE Trans. Ind. Electron., vol. 60, no. 2, pp. 781–788, Feb. 2013.

[23] S. M. Tayebi, and I. Batarseh, "Mitigation of Current Distortion in a Three-Phase Microinverter With Phase Skipping Using a Synchronous Sampling DC-Link Voltage Control," IEEE Trans. Ind. Electron., vol. 65, no. 5, pp.3910–3920, May. 2018.

[24] X. Zhao, L. Zhang, R. Born, and J. Lai, "A High-Efficiency Hybrid Resonant Converter With Wide-Input Regulation for Photovoltaic Applications," IEEE Trans. Ind. Electron., vol. 64, no. 5, pp.3684–3695, May. 2017.

[25] A. Trubitsyn, B. J. Pierquet, A. K. Hayman, G E. Gamache, C. R. Sullivan, D. J. Perreault "High-Efficiency Inverter for Photovoltaic Applications," in Proc. IEEE Energy Conversion Congress and Exposition Conf., Jun. 2010, pp. 2803–2810.

[26] C. Felgemacher, . Jager, A. Kobeissi, J. Pfeiffer, D. Wiegand, W. Kruschel, B. Dombert, S. V. Araujo, and P. Zacharias, "Design of Photovoltaic Microinverter for Off-Grid and Grid-Parallel Applications," in Proc. IEEE. Integrated Power Electronics Systems Conf., Feb. 2014, pp. 1–6.

[27] A. C. Nanakos, E. C. Tatakis, and N. P. Papanikolaou, "A Weighted-Efficiency-Oriented Design Methodology of Flyback Inverter for AC Photovoltaic Modules," IEEE Trans. Power Electron., vol. 27, no. 7, pp. 3221–3233, Jul. 2012.

[28] A. C. Nanakos, G. C. Christidis, and E. C. Tatakis, "Weighted Efficiency Optimization of Flyback Microinverter Under Improved Boundary Conduction Mode (i-BCM)," IEEE Trans. Power Electron., vol. 30, no. 10, pp. 5548–5564, Jun. 2015.

[29] Y. Kim, Y. Ji, J. Kim, Y. Jung, and C. Won, "A New Control Strategy for Improving Weighted Efficiency in Photovoltaic AC Module-Type Interleaved Flyback Inverters," IEEE Trans. Power Electron., vol. 28, no. 6, pp. 2688–2699, Jun. 2013.

[30] Y. Kim, J. Jang, S. Shin, and C. Won, "Weighted-Efficiency Enhancement Control for a Photovoltaic AC Module Interleaved Flyback Inverter Using a Synchronous Rectifier," IEEE Trans. Power Electron., vol. 29, no. 12, pp. 6481–6493, Dec. 2014.

[31] Z. Zhang, X. He, and Y. Liu, "An Optimal Control Method for Photovoltaic Grid-Tied-Interleaved Flyback Microinverters to Achieve High Efficiency in Wide Load Range," IEEE Trans. Power Electron., vol. 28, no. 11, pp. 5074–5087, Nov. 2013.

[32] Y. Levron, and Robert W. Erickson, "High Weighted Efficiency in Single-Phase Solar Inverters by a Variable-Frequency Peak Current Controller," IEEE Trans. Power Electron., vol. 31, no. 1, pp. 6481–6493, Jan. 2016.

[33] S. Poshtkouhi, and O. Trescases, "Flyback Mode for Improved Low-Power Efficiency in the Dual-Active-Bridge Converter for Bidirectional PV Microinverters With Integrated Storage," IEEE Trans. Ind. Appl., vol. 51, no. 4, pp. 3316–3324, Jul./Aug. 2015.

[34] M. Gao, M. Chen, C. Zhang, and Z. Qian, "Analysis and Implementation of an Improved Flyback Inverter for Photovoltaic AC Module Applications," IEEE Trans. Power Electron., vol. 29, no. 7, pp. 3428–3444, Jul. 2014.

[35] M. A. Rezaei, K. Lee, and Alex Q. Huang, "A High-Efficiency Flyback Micro-inverter With a New Adaptive Snubber for Photovoltaic

Applications," IEEE Trans. Power Electron., vol. 31, no. 1, pp. 318–327, Jan. 2016.

[36] N. Sukesh, M. Pahlevaninezhad, and P. K. Jain, "Analysis and Implementation of a Single-Stage Flyback PV Microinverter With Soft Switching," IEEE Trans. Ind. Electron., vol. 61, no. 4, pp. 1819–1833, Apr. 2014.

[37] G. C. Christidis, A. Ch. Nanakos, and E. C. Tatakis, "Hybrid Discontinuous/Boundary Conduction Mode of Flyback Microinverter for AC–PV Modules," IEEE Trans. Power Electron., vol. 31, no. 6, pp. 4195–4205, Jan. 2016.

[38] J. M. Alonso, M. S. Perdigao, D. G. Vaquero, A. J. Calleja, and E. S. Saraiva, "Analysis, Design, and Experimentation on Constant-Frequency DC-DC Resonant Converters With Magnetic Control," IEEE Trans. Power Electron., vol. 27, no. 3, pp. 4195–4205, Mar. 2012.

[39] D. Medini and S. Ben-Yaakov, "A current-controlled variable inductor for high frequency resonant power circuits," in Proc. IEEE APEC, 1994, pp. 219–225.

[40] H. Fan and H. Li, "A novel phase-shift bidirectional dc–dc converter with an extended high-efficiency range for 20 kVA solid state transformer," in Proc. IEEE ECCE, Sep. 2010, pp. 3870–3876.

[41] Jinming Xu, Shaojun Xie, Jiarong Kan, Binfeng Zhang, "Research on Stability of Grid-Connected LCL Filtered Inverter with Capacitor Current Feedback Active Damping Control," in Proc. International Conference on Power Electronics Conf., Jun. 2015, pp. 682–687.

This work was supported by the National Natural Science Foundation of China under Grants 51577164, 51107108, and by Jiangsu Province fifth "333 Project" Research Project, and by six talent peaks project in Jiangsu Province(XNY-045).

The corresponding author is Yu TANG.

J. Kan and Y. Wu are with the College of Electrical Engineering, Yancheng Institute of Technology, Yancheng, 224051, China (e-mail: kanjr@163.com; wuyunyayi@163.com).

Y. Tang is with the State Key Laboratory of Reliability and Intelligence of Electrical Equipment（Hebei University of Technology） & Key Laboratory of Electromagnetic Field and Electrical Apparatus Reliability of Hebei Province(Hebei University of Technology), Tianjin, 300401, China (e-mail: ty8025@hotmail.com).

S. Xie is with the College of Automation Engineering, Nanjing University of Aeronautics and

Astronautics, Nanjing 210016, China (e-mail: eeac@nuaa.edu.cn).

L. Jiang is with the Department of Electrical Engineering and Electronics, The University of Liverpool, Liverpool L69 3GJ, U.K. (e-mail: ljiang@liv.ac.uk).